

Fusion Enhancement for Neutron-Rich Light Nuclei

Varinderjit Singh, J. Vadas, T. K. Steinbach, S. Hudan, and R. T. deSouza*

*Department of Chemistry and Center for Exploration of Energy and Matter, Indiana University
2401 Milo B. Sampson Lane, Bloomington, Indiana 47408 USA*

L. T. Baby, S. A. Kuvin, V. Tripathi, and I. Wiedenhöver

Department of Physics, Florida State University, Tallahassee, Florida, 32306 USA

(Dated: March 31, 2016)

Background Measurement of the fusion cross-section for neutron-rich light nuclei is crucial in ascertaining if fusion of these nuclei occurs in the outer crust of a neutron star.

Purpose Measure the fusion excitation function at near-barrier energies for the $^{19}\text{O} + ^{12}\text{C}$ system. Compare the experimental results with the fusion excitation function of $^{18}\text{O} + ^{12}\text{C}$ and $^{16}\text{O} + ^{12}\text{C}$.

Method A beam of ^{19}O , produced via the $^{18}\text{O}(\text{d},\text{p})$ reaction, was incident on a ^{12}C target at energies near the Coulomb barrier. Evaporation residues produced in fusion of $^{18,19}\text{O}$ ions with ^{12}C target nuclei were detected with good geometric efficiency and identified by measuring their energy and time-of-flight.

Results A significant enhancement is observed in the fusion probability of ^{19}O ions with a ^{12}C target as compared to ^{18}O ions.

Conclusion The larger cross-sections observed at near barrier energies is related to significant narrowing of the fusion barrier indicating a larger tunneling probability for the fusion process.

PACS numbers: 26.60.Gj, 25.60.Pj, 25.70.Jj

Approximately half the elements beyond iron are formed via the r-process in which seed nuclei rapidly capture multiple neutrons and subsequently undergo β decay. Although it is clear that a high neutron density is required for the r-process, the exact site or sites at which r-process nucleosynthesis occurs is still a question of debate. One proposed scenario involves the merging of two compact objects such as neutron stars. Tidal forces between the two compact objects disrupts the neutron stars, ejecting neutron-rich nuclei into the interstellar medium. Although nucleosynthesis via decompression of neutronized nuclear matter was initially proposed decades ago [1, 2], only recently have detailed computational investigations of such a scenario e.g. tidal disruption of a neutron star become feasible [3–7]. The most recent calculations suggest that such events could be responsible for heavy element ($A > 130$) r-process nucleosynthesis. Recent observation of gravitational waves emanating from two black holes merging [8] has re-ignited the question of whether and to what degree the disruption of neutron stars contributes to the heavy element composition of the universe.

A natural question in considering the ejecta from the disruption of the neutron star is the composition of the neutron star prior to the merger as well as the reactions that might occur both during and post the merging event. The outer crust of a neutron star provides an unique environment in which nuclear reactions can occur. Of particular interest are the fusion reactions of neutron-rich light nuclei. These nuclei have been hypothesized to fuse more readily than the corresponding β stable isotopes

providing a potential heat source that triggers the fusion of ^{12}C nuclei resulting in an X-ray superburst [9]. An initial measurement of fusion induced with neutron-rich oxygen nuclei suggested an enhancement of the fusion probability as compared to standard models of fusion-evaporation [10]. To definitively establish if neutron-rich light nuclei exhibit a fusion enhancement at sub-barrier energies, high quality experimental data is needed. In the present work, we present for the first time a measurement of the total fusion cross-section for $^{19}\text{O} + ^{12}\text{C}$ at incident energies near the barrier and compare the results with the fusion cross-section for $^{16,18}\text{O} + ^{12}\text{C}$.

Fusion excitation functions reflect the interplay of the repulsive Coulomb and attractive nuclear potentials as the two nuclei collide. As the charge distribution of the projectile oxygen nuclei is essentially unaffected by the additional neutrons, the repulsive Coulomb potential is unchanged. Consequently, the comparison of the fusion excitation functions for the different oxygen isotopes provides access to the changes in the attractive nuclear potential. This change in the attractive potential can be related to changes in the neutron density distribution with increasing number of neutrons for oxygen nuclei.

The experiment was performed at the John D. Fox accelerator laboratory at Florida State University. A beam of ^{18}O ions, accelerated to an energy of 80.7 MeV impinged on a deuterium gas cell at a pressure of 350 torr cooled to a temperature of 77 K. Ions of ^{19}O were produced via a (d,p) reaction and separated from the incident beam by the electromagnetic spectrometer RESO-LUT [11]. Although this spectrometer rejected most of the unreacted beam that exited the production gas cell, the beam exiting the spectrometer consisted of both ^{19}O and ^{18}O ions. As each beam particle was independently identified, this beam mixture allowed simultaneous mea-

*Electronic address: desouza@indiana.edu

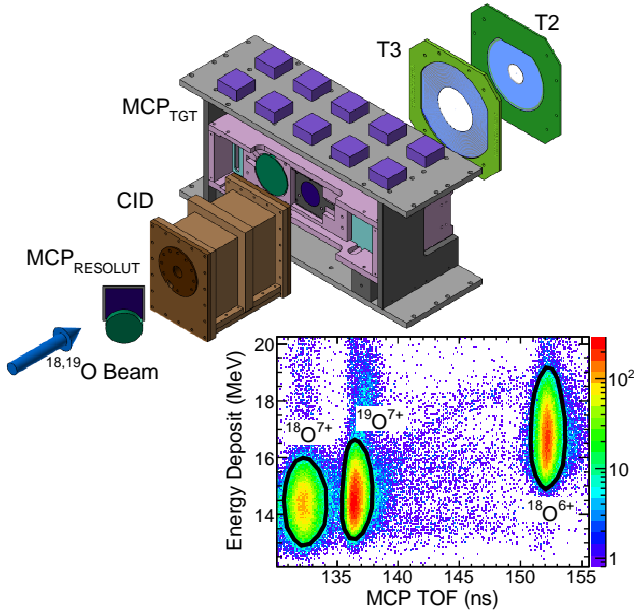


FIG. 1: (Color online) Schematic illustration of the experimental setup. The MCP_{RESOLUT} detector is located approximately 3.5 m upstream of the MCP_{TGT} detector. Inset: Energy deposit versus time-of-flight spectrum for ions exiting RESOLUT that are incident on ^{12}C target at $E_{\text{lab}}=46.7$ MeV. Color is used to represent yield in the two dimensional spectrum on a logarithmic scale.

surement of $^{18}\text{O} + ^{12}\text{C}$ and $^{19}\text{O} + ^{12}\text{C}$ thus providing a robust measure of the fusion enhancement due to the presence of the additional neutron. The experimental setup used to measure fusion of oxygen ions with carbon nuclei is depicted in Fig. 1. To identify beam particles, the energy deposit and time-of-flight [12] of each particle was measured. Upon exiting the spectrometer particles first traverse a thin secondary emission foil (0.5 μm thick aluminized mylar) ejecting electrons in the process. These electrons are accelerated and bent out of the beam path and onto the surface of a microchannel plate detector (MCP_{RESOLUT}) where they are amplified to produce a fast timing signal. After traversing the thin foil of MCP_{RESOLUT}, the ions passed through a compact ionization detector (CID) located approximately 3.5 m downstream. Passage of the ions through this ionization chamber results in an energy deposit (ΔE) characterized by their atomic number (Z), mass number (A), and incident energy. After exiting the small ionization chamber the ions are incident on a 100 $\mu\text{g}/\text{cm}^2$ carbon foil. This foil serves both as a secondary electron emission foil for the target microchannel plate detector (MCP_{TGT}) and as the target for the fusion experiment.

By utilizing the timing signals from both microchannel plate detectors together with the ionization chamber a ΔE -TOF measurement is performed. This measurement allows identification of ions in the beam as indicated in the inset of Fig. 1. Clearly evident in the figure are three peaks associated with the $^{19}\text{O}^{7+}$ ions, $^{18}\text{O}^{7+}$ ions, and

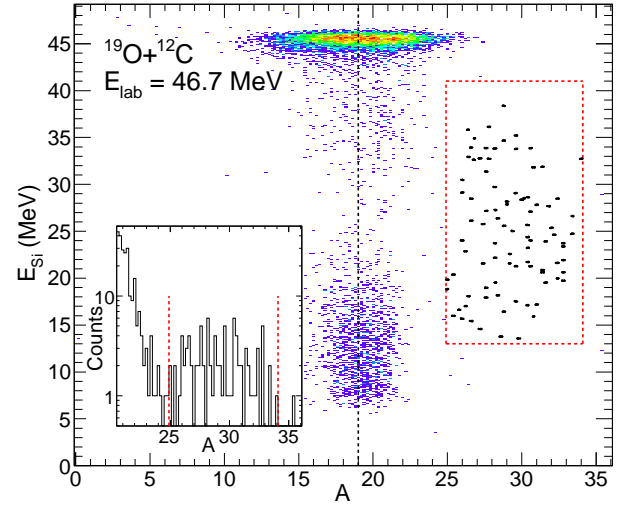


FIG. 2: (Color online) Two dimensional spectrum depicting dependence of the energy deposited in the annular silicon detector, T2, on the mass of the ion. The dashed (red) rectangle indicates the region of the evaporation residues. Inset: Mass distribution of ions detected within the interval $13 \text{ MeV} < E_{Si} < 41 \text{ MeV}$. Vertical lines indicate the A limits used to designate evaporation residues.

$^{18}\text{O}^{6+}$ ions. The ^{19}O ions corresponded to 31 % of the beam intensity with the $^{18}\text{O}^{7+}$ and $^{18}\text{O}^{6+}$ corresponding to approximately 20 % and 29 % respectively. Fusion of ^{19}O (or ^{18}O) nuclei in the beam together with ^{12}C nuclei in the target foil results in the production of an excited ^{31}Si (or correspondingly ^{30}Si) nucleus. For collisions near the Coulomb barrier the excitation of the fusion product is relatively modest, $E^* \approx 35$ MeV. This fusion product de-excites by evaporation of a few neutrons, protons, and α particles resulting in evaporation residues (ERs). Statistical model calculations [13] indicate that for ^{31}Si compound nucleus, the nuclei ^{30}Si , ^{29}Si , ^{28}Si , ^{29}Al , ^{28}Al , ^{27}Mg , and ^{26}Mg account for the bulk of the ERs. These ERs are deflected from the beam direction by the recoil imparted by the emission of the light particles. The ERs are detected and identified by two annular silicon detectors designated T2 and T3 situated downstream of the MCP_{TGT}. These detectors subtend the angular range $3.5^\circ < \theta_{\text{lab}} < 25^\circ$. Evaporation residues are distinguished from scattered beam, as well as emitted light particles, by measuring their time-of-flight between the MCP_{TGT} detector and the silicon detectors together with the energy deposit in the Si detector, E_{Si} . Using the measured energy deposit, E_{Si} and the time-of-flight, the mass of the ion can be calculated. Shown in Fig. 2 is the representative two-dimensional mass-energy distribution for particles incident on the T2 detector at an incident energy in the laboratory of 46.7 MeV for $^{19}\text{O}^{7+}$ beam. The most prominent feature of this spectrum is the peak at $E_{Si} = 45$ MeV and $A=19$ which corresponds to elastically scattered beam particles. At lower energies than this peak with a mass centered on $A=19$ one also observes

a ridge of intensity corresponding to beam particles that are scattered in the experimental setup downstream of the target but prior to entering the silicon detector. This scattered beam corresponds to approximately 15 % of the elastic peak intensity. Situated at higher mass number than the scattered beam and with energies $13 \text{ MeV} < E_{Si} < 41 \text{ MeV}$ are detected ions that correspond to evaporation residues. The mass distribution associated with this energy interval is presented in the inset of Fig. 2. A clear peak in the mass distribution is evident at $A < 30$. The peak is clearly separated from the tail of the scattered beam particles. The centroid and second moment of this peak was determined in the interval $24.5 < A < 34$. The measured $\langle A \rangle$ for the evaporation residues is 29 and the second moment σ_{ER} measured = 2.32. The measured width of the evaporation residue mass resolution is largely dictated by the time and energy resolution of the measurement as is evident from the width of the elastic peak ($\sigma_{elastic} = 2.44$).

The fusion cross-section is extracted from the measured yield of evaporation residues through the relation $\sigma_{fusion} = N_{ER} / (\epsilon_{ER} \times t \times N_{INCIDENT})$ where $N_{INCIDENT}$ is the number of beam particles of a given type incident on the target, t is the target thickness, ϵ_{ER} is the detection efficiency, and N_{ER} is the number of evaporation residues detected. The number $N_{INCIDENT}$ is determined by counting the particles with the appropriate time-of-flight between the two microchannel plates that additionally have the correct identification in the ΔE -TOF map depicted in the inset of Fig. 1. The target thickness, t , of $105 \mu\text{g}/\text{cm}^2$ is provided by the manufacturer and has an uncertainty of $\pm 0.5 \mu\text{g}/\text{cm}^2$. The number of detected residues, N_{ER} , is determined by summing the number of detected residues with the appropriate mass and energy as indicated in Fig. 2. To obtain the detection efficiency, ϵ_{ER} , a statistical model is used to describe the de-excitation of the fusion product together with the geometric acceptance of the experimental setup. The detection efficiency varied from 37 % at the highest incident energies measured to 42 % at the lowest incident energy due to the changing kinematics of the reaction.

Presented in Fig. 3 is the dependence of the fusion cross-section on incident energy for $^{19}\text{O} + ^{12}\text{C}$ (red triangles) and $^{18}\text{O} + ^{12}\text{C}$ (blue triangles) measured in the present experiment. Also shown for comparison is a prior high resolution measurement (open triangles) [14] together with older data from the literature [15] for $^{18}\text{O} + ^{12}\text{C}$. This high resolution measurement utilized a direct high quality beam of ^{18}O with a similar experimental setup to the present experiment [14, 16]. It is clear from Fig. 3 that the measured cross-section for the ^{18}O beam in the present experiment (blue points) is in good agreement with the previous high resolution measurements (open triangles and squares). This result provides confidence in the radioactive beam cross-sections simultaneously measured in the present experiment. Also shown in Fig. 3 (open circles) is the fusion excitation function for $^{16}\text{O} + ^{12}\text{C}$. The data presented utilizes only direct

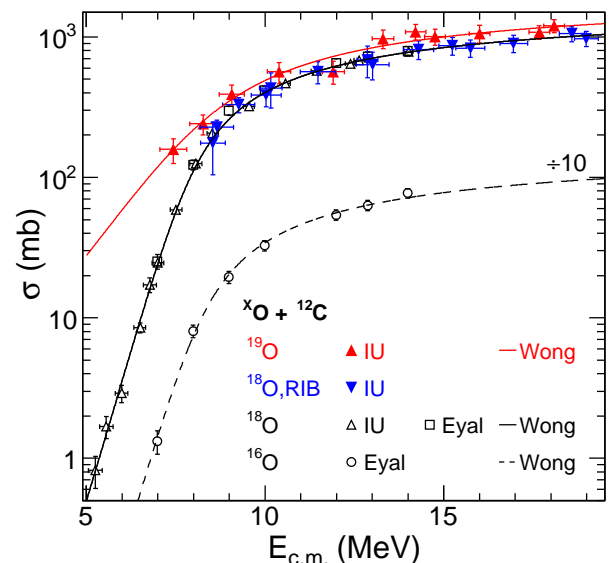


FIG. 3: (Color online) Fusion excitation function for $^{16,18,19}\text{O}$ ions incident on ^{12}C target nuclei. The data for $^{16}\text{O} + ^{12}\text{C}$ have been scaled down by a factor of 10.

measurement of evaporation residues [15] to characterize the excitation function. This excitation function has also been measured by detection of γ rays in a thick-target experiment. The data from that experiment [17] is in reasonably good agreement with the excitation function depicted. However, as use of the thick target measurements is subject to different uncertainties, we omit these data in order to make the most straightforward and relevant comparison.

All of the excitation functions depicted in Fig. 3 manifest the same general trend. With decreasing incident energy the cross-section decreases as expected for a barrier controlled process. Closer examination of the ^{19}O and ^{18}O reactions reveals that the ^{19}O data exhibits a larger fusion cross-section as compared to the ^{18}O data at essentially all energies measured. The most important feature of the measured excitation functions is that at the lowest energies measured the fusion cross-section for the ^{19}O system decreases more gradually with decreasing energy than does the ^{18}O system. In order to better quantify these differences in the fusion excitation functions we have fit the measured cross-sections with a simple one dimensional barrier penetration model. The Wong formalism [18] considers the penetration of an inverted parabolic barrier with the cross-section given by:

$$\sigma = \frac{R_C^2}{2E} \hbar\omega \cdot \ln \left\{ 1 + \exp \left[\frac{2\pi}{\hbar\omega} (E - V_C) \right] \right\} \quad (1)$$

where E is the incident energy, V_C is the barrier height, R_C is the radius of interaction and $\hbar\omega$ is the barrier curvature. The fit of the high resolution ^{18}O data and the ^{16}O data are indicated as the solid black and dashed black lines in Fig. 3 respectively. The good agreement observed between the Wong fit of the high resolution ^{18}O data and

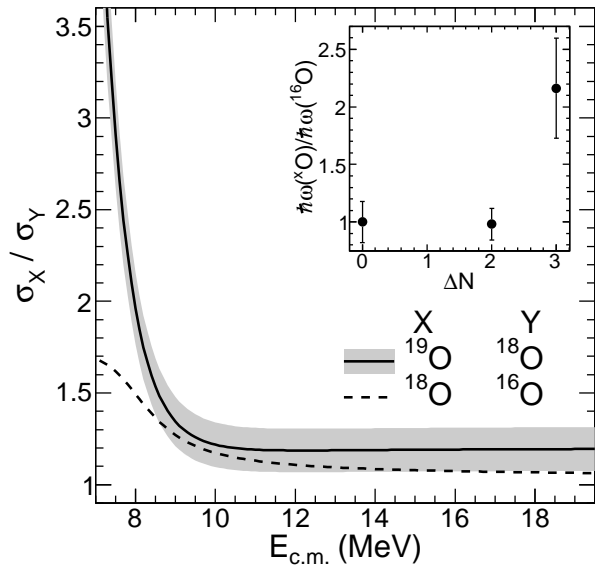


FIG. 4: Dependence of the ratio of $\sigma(^{19}\text{O})/\sigma(^{18}\text{O})$ and $\sigma(^{18}\text{O})/\sigma(^{16}\text{O})$ on $E_{c.m.}$. The shaded region depicts the uncertainty associated with the ratio for the ^{19}O reaction. Inset: Dependence of the ratio of the barrier curvature on neutron number for the ^{19}O and ^{18}O reactions as compared to the ^{16}O reaction.

the ^{18}O data measured in this experiment (blue points) underscores that there are no significant systematic errors associated with the present measurement. The solid red curve in Fig. 3 depicts the fit of the ^{19}O data. With the exception of the cross-section measured at $E_{cm} \approx 12$ MeV, the measured cross-sections are reasonably described by the Wong formalism. The extracted parameters for the ^{16}O , ^{18}O , and ^{19}O reactions are summarized in Table 1. It is not surprising that the barrier height, V_C , remains essentially the same for all of the three reactions examined as the charge density distribution is unchanged.

TABLE I: Wong fit parameters for the indicated fusion excitation functions. See text for details.

	V_C (MeV)	R_C (fm)	$\hbar\omega$ (MeV)
$^{16}\text{O} + ^{12}\text{C}$	7.93 ± 0.16	7.25 ± 0.25	2.95 ± 0.37
$^{18}\text{O} + ^{12}\text{C}$	7.66 ± 0.10	7.39 ± 0.11	2.90 ± 0.18
$^{19}\text{O} + ^{12}\text{C}$	7.73 ± 0.72	8.10 ± 0.47	6.38 ± 1.00

The dependence of the ratio $\sigma(^{19}\text{O})/\sigma(^{18}\text{O})$ and $\sigma(^{18}\text{O})/\sigma(^{16}\text{O})$ on $E_{c.m.}$ is shown in Fig. 4. The solid line corresponds to the ratio of the Wong fit for ^{19}O to the Wong fit for ^{18}O . For $E_{c.m.} > 10$ MeV, this ratio is essentially constant at a value of approximately 1.2. For $E_{c.m.} < 10$ MeV, the quantity $\sigma(^{19}\text{O})/\sigma(^{18}\text{O})$ increases rapidly reaching a value of ≈ 3.0 at the lowest energy measured. It is useful to examine the behavior of $\sigma(^{18}\text{O})/\sigma(^{16}\text{O})$ presented as the dashed line in Fig. 4. for comparison. At energies well above the barrier $\sigma(^{18}\text{O})/\sigma(^{16}\text{O})$ is es-

entially flat at a value of ≈ 1.1 . As one approaches the barrier it increases to a value of approximately 1.7. Hence the enhancement observed for ^{19}O is significantly larger than in the case of ^{18}O .

In the energy domain above the barrier one expects the ratio of the two cross-sections to be governed by the ratio of their geometric cross-sections namely the square of the ratio of their radii. The 20% increase in the cross-section observed for ^{19}O relative to ^{18}O can thus be associated with a larger radius for ^{19}O as compared to ^{18}O within the framework of an inverted parabolic barrier penetration model. The magnitude of the increase in R_C , for the ^{19}O reaction as compared to the ^{18}O reaction, is 0.71 fm, which corresponds to a relative increase of approximately 10%. This increase is significantly larger than the increase of 0.14 fm for ^{18}O reaction as compared to ^{16}O . This increase in the radius is significantly larger than that expected based upon a standard $A^{1/3}$ dependence emphasizing the fact that in these low energy fusion reactions, the initial interpenetration of the matter distributions of the two nuclei is small. Consequently, it is the interaction between the two low-density tails of the colliding nuclei that governs whether the fusion occurs. As the $A^{1/3}$ dependence does not describe the behavior of the low-density tail it is unsurprising that the experimental data deviates from this behavior.

Near and below the barrier, one expects the cross-section to be governed by the detailed shape of the barrier. Within the context of the Wong formalism this is reflected by the barrier curvature, $\hbar\omega$. Shown in the inset of Fig. 4 is the curvature of the barrier for $^{18,19}\text{O} + ^{12}\text{C}$ as compared to $^{16}\text{O} + ^{12}\text{C}$ as a function of additional neutrons. It is clearly evident that while the additional two neutrons in ^{18}O as compared to ^{16}O do not substantially alter the barrier curvature, the presence of the additional unpaired neutron in ^{19}O significantly increases the barrier curvature. The barrier in the case of ^{19}O is a factor of 2.2 thinner than in the case of ^{16}O resulting in greater penetration and an enhancement of the fusion cross-section. Although the success of static models in describing the fusion of stable light nuclei is well established, it is unclear whether fusion of neutron-rich nuclei necessitates consideration of collective modes i.e. dynamics as the two nuclei fuse. Comparison of the present experimental data with more sophisticated models such as a density constrained TDHF model [19] are presently underway.

In summary, we have measured for the first time the fusion of $^{19}\text{O} + ^{12}\text{C}$ at incident energies near and below the barrier. This measurement probes the open question of whether fusion of light neutron-rich nuclei is enhanced relative to their β stable isotopes. Comparison of the fusion excitation function for $^{19}\text{O} + ^{12}\text{C}$ with that of $^{18}\text{O} + ^{12}\text{C}$, clearly demonstrates that for the ^{19}O system, fusion is significantly enhanced. Well above the barrier this enhancement is approximately 20 % which can be related to an increase in the radius of $\approx 10\%$ due just to the presence of the additional neutron. Near and below the

barrier the fusion enhancement is even more dramatic, increasing to a factor of three at the lowest energy measured. The dramatic increase in this energy domain is related to a significant reduction in the width of the fusion barrier for ^{19}O as compared to ^{18}O . Within the context of an inverted parabolic model the barrier for ^{19}O is 2.2 times narrower than that for ^{18}O . The decrease in the width of the barrier with increasing neutron number suggests that even more neutron-rich oxygen isotopes may exhibit even narrower barriers and larger fusion enhancements. These results motivate the investigation of even more neutron-rich light nuclei, particularly at energies

near and below the barrier.

We wish to acknowledge the support of the staff at Florida State University's John D. Fox accelerator in providing the high quality beam that made this experiment possible. This work was supported by the U.S. Department of Energy under Grant No. DE-FG02-88ER-40404 (Indiana University), Grant no. DE-FG02-02ER-41220 (Florida State University) and the National Science Foundation under Grant No PHY-1491574 (Florida State University). J.V. acknowledges the support of a NSF Graduate Research Fellowship under Grant No. 1342962.

-
- [1] J. M. Lattimer et al., *Astrophysical Journal* **213**, 225 (1977).
 - [2] B. S. Meyer et al., *Astrophysical Journal* **343**, 254 (1989).
 - [3] E. Berger, W. Fong, and R. Chornock, *The Astrophysical Journal Letters* **774**, L23 (2013).
 - [4] D. Martin et al., *Nucleosynthesis in the ejecta of neutron star mergers* (2015), arXiv:1509.07628.
 - [5] F. Foucart et al., *Phys. Rev. D* **90**, 024026 (2014).
 - [6] O. Just et al., *Mon. Not. Roy. Astr. Soc.* **448**, 541 (2015).
 - [7] D. Radice et al. (2016), arXiv:1601.02426v1.
 - [8] B. P. Abbott et al., *Phys. Rev. Lett.* **116**, 061102 (2016).
 - [9] C. J. Horowitz, H. Dussan, and D. K. Berry, *Phys. Rev. C* **77**, 045807 (2008).
 - [10] M. J. Rudolph et al., *Phys. Rev. C* **85**, 024605 (R) (2012).
 - [11] I. Wiedenhöver et al., in *Fifth International Conference on Fission and Properties of Neutron-rich Nuclei*, edited by J. Hamilton and A. Ramayya (World Scientific, 2012), ISBN 978-981-4525-42-8.
 - [12] R. T. deSouza et al., *Nucl. Instr. and Meth.* **A632**, 133 (2011).
 - [13] N. G. Nicolis and J. R. Beene, unpublished (1993).
 - [14] T. K. Steinbach et al., *Phys. Rev. C* **90**, 041603(R) (2014).
 - [15] Y. Eyal, M. Beckerman, R. Checkhik, Z. Fraenkel, and H. Stocker, *Phys. Rev. C* **13**, 1527 (1976).
 - [16] T. K. Steinbach et al., *Nucl. Instr. and Meth.* **A743**, 5 (2014).
 - [17] B. Cujec and C. A. Barnes, *Nucl. Phys. A* **266**, 461 (1976).
 - [18] C. Y. Wong, *Phys. Rev. Lett.* **31**, 766 (1973).
 - [19] R. Keser, A. S. Umar, and V. E. Oberacker, *Phys. Rev. C* **85**, 044606 (2012).